Pergamon

Carbon, Vol. 33, No. 7, pp. 893-902, 1995

0008-6223/95 $9.50 + .00

0008-6223(95)00018-6

ELECTRONIC AND STRUCTURAL PROPERTIES OF CARBON NANOTUBES

J. W. MINTMIRE and C. T. WHITE
Chemistry Division, Naval Research Laboratory, Washington, DC 20375-5342, U.S.A.

(*Received* 12 *October* 1994; *accepted in revised form* 15 *February* 1995)

Abstract—Recent developments using synthetic methods typical of fullerene production have been used to generate graphitic nanotubes with diameters on the order of fullerene diameters: "carbon nanotubes." The individual hollow concentric graphitic nanotubes that comprise these fibers can be visualized as constructed from rolled-up single sheets of graphite. We discuss the use of helical symmetry for the electronic structure of these nanotubes, and the resulting trends we observe in both band gap and strain energy versus nanotube radius, using both empirical and first-principles techniques. With potential electronic and structural applications, these materials appear to be appropriate synthetic targets for the current decade.

Key Words—Carbon nanotube, electronic properties, structural properties, strain energy, band gap, band structure, electronic structure.

1. INTRODUCTION

Less than four years ago Iijima[1] reported the novel synthesis based on the techniques used for fullerene synthesis[2,3] of substantial quantities of multiple-shell graphitic nanotubes with diameters of nanometer dimensions. These nanotube diameters were more than an order of magnitude smaller than those typically obtained using routine synthetic methods for graphite fibers[4,5]. This work has been widely confirmed in the literature, with subsequent work by Ebbesen and Ajayan[6] demonstrating the synthesis of bulk quantities of these materials. More recent work has further demonstrated the synthesis of abundant amounts of single-shell graphitic nanotubes with diameters on the order of one nanometer[7-9]. Concurrent with these experimental studies, there have been many theoretical studies of the mechanical and electronic properties of these novel fibers[10-30]. Already, theoretical studies of the individual hollow concentric graphitic nanotubes, which comprise these fibers, predict that these nanometer-scale diameter nanotubes will exhibit conducting properties ranging from metals to moderate bandgap semiconductors, depending on their radii and helical structure[10-22]. Other theoretical studies have focused on structural properties and have suggested that these nanotubes could have high strengths and rigidity resulting from their graphitic and tubular structure[23-30]. The metallic nanotubes—termed serpentine[23]—have also been predicted to be stable against a Peierls distortion to temperatures far below room temperature[10]. The fullerene nanotubes show the promise of an array of all-carbon structures that exhibits a broad range of electronic and structural properties, making these materials an important synthetic target for the current decade.

Herein, we summarize some of the basic electronic and structural properties expected of these nanotubes from theoretical grounds. First we will discuss the basic structures of the nanotubes, define the nomenclature used in the rest of the manuscript, and present an analysis of the rotational and helical symmetries of the nanotube. Then, we will discuss the electronic structure of the nanotubes in terms of applying Born-von Karman boundary conditions to the two-dimensional graphene sheet. We will then discuss changes introduced by treating the nanotube realistically as a three-dimensional system with helicity, including results both from all-valence empirical tight-binding results and first-principles local-density functional (LDF) results.

2. NANOTUBE STRUCTURE AND SYMMETRY

Each single-walled nanotube can be viewed as a conformal mapping of the two-dimensional lattice of a single sheet of graphite (graphene), depicted as the honeycomb lattice of a single layer of graphite in Fig. 1, onto the surface of a cylinder. As pointed out by Iijima[1], the proper boundary conditions around the cylinder can only be satisfied if one of the Bravais lattice vectors of the graphite sheet maps to a circumference around the cylinder. Thus, each real lattice vector of the two-dimensional hexagonal lattice (the Bravais lattice for the honeycomb) defines a different way of rolling up the sheet into a nanotube. Each such lattice vector, $\mathbf{B}$, can be defined in terms of the two primitive lattice vectors $\mathbf{R}_1$ and $\mathbf{R}_2$ and a pair of integer indices $[n_1, n_2]$, such that $\mathbf{B} = n_1\mathbf{R}_1 + n_2\mathbf{R}_2$, with Fig. 2 depicting an example for a [4,3] nanotube. The point group symmetry of the honeycomb lattice will make many of these equivalent, however, so truly unique nanotubes are only generated using a one-twelfth irreducible wedge of the Bravais lattice. Within this wedge, only a finite number of nanotubes can be constructed with a circumference below any given value.

The construction of the nanotube from a conformal mapping of the graphite sheet shows that each nanotube can have up to three inequivalent (by point

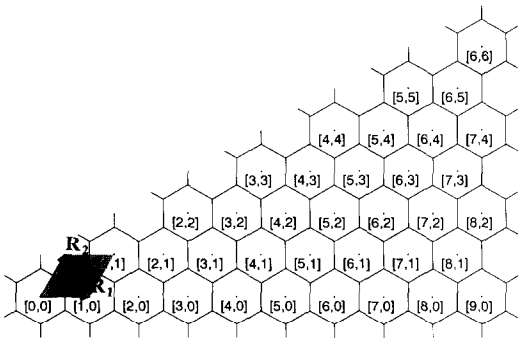

Fig. 1. Two-dimensional honeycomb lattice of graphene; primitive lattice vectors $\mathbf{R}_1$ and $\mathbf{R}_2$ are depicted outlining primitive unit cell.

group symmetry) helical operations derived from the primitive lattice vectors of the graphite sheet. Thus, while *all* nanotubes have a helical structure, nanotubes constructed by mapping directions equivalent to lattice translation indices of the form $[n,0]$ and $[n,n]$, to the circumference of the nanotube will possess a reflection plane. These high-symmetry nanotubes will, therefore, be achiral[12–14,23]. For convenience, we have labeled these special structures based on the shapes made by the most direct continuous path of bonds around the circumference of the nanotube[23]. Specifically, the $[n,0]$-type structures were labeled as sawtooth and the $[n,n]$-type structures as serpentine. For all other conformations inequivalent to these two sets, the nanotubes are chiral and have three inequivalent helical operations.

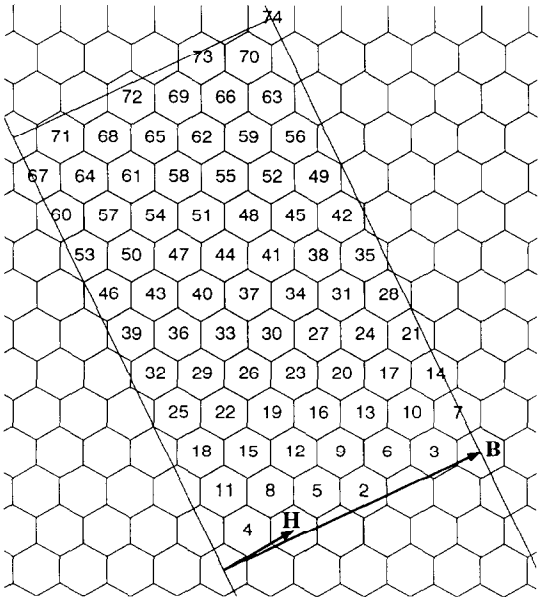

Fig. 2. Depiction of conformal mapping of graphene lattice to [4,3] nanotube. **B** denotes [4,3] lattice vector that transforms to circumference of nanotube, and **H** transforms into the helical operator yielding the minimum unit cell size under helical symmetry. The numerals indicate the ordering of the helical steps necessary to obtain one-dimensional translation periodicity.

Because real lattice vectors can be found that are normal to the primitive real lattice vectors for the graphite sheet, each nanotube thus generated can be shown to be translationally periodic down the nanotube axis[12–14,23]. However, even for relatively small diameter nanotubes, the minimum number of atoms in a translational unit cell can be quite large. For example, for the [4,3] nanotube ($n_1 = 4$ and $n_2 = 3$) then the radius of the nanotube is less than 0.3 nm, but the translational unit cell contains 148 carbon atoms as depicted in Fig. 2. The rapid growth in the number of atoms that can occur in the minimum translational unit cell makes recourse to the helical and any higher point group symmetry of these nanotubes practically mandatory in any comprehensive study of their properties as a function of radius and helicity. These symmetries can be used to reduce to two the number of atoms necessary to generate any nanotube[13,14]; for example, reducing the matrices that have to be diagonalized in a calculation of the nanotube's electronic structure to a size no larger than that encountered in a corresponding electronic structure calculation of two-dimensional graphene.

Before we can analyze the electronic structure of a nanotube in terms of its helical symmetry, we need to find an appropriate helical operator $\mathbb{S}(h,\varphi)$, representing a screw operation with a translation h units along the cylinder axis in conjunction with a rotation φ radians about this axis. We also wish to find the operator $\mathbb{S}$ that requires the minimum unit cell size (i.e., the smallest set of carbon atoms needed to generate the entire nanotube using $\mathbb{S}$) to minimize the computational complexity of calculating the electronic structure. We can find this helical operator $\mathbb{S}(h,\varphi)$ by first finding the real lattice vector $\mathbf{H} = m_1\mathbf{R}_1 + m_2\mathbf{R}_2$ in the honeycomb lattice that will transform to $\mathbb{S}(h,\varphi)$ under conformal mapping, such that $h = |\mathbf{H}\times\mathbf{B}|/|\mathbf{B}|$ and $\varphi = 2\pi(\mathbf{H}\cdot\mathbf{B})/|\mathbf{B}|^2$. An example of $\mathbf{H}$ is depicted in Fig. 2 for the [4,3] nanotube. If we construct the cross product $\mathbf{H}\times\mathbf{B}$ of $\mathbf{H}$ and $\mathbf{B}$, the magnitude $|\mathbf{H}\times\mathbf{B}|$ will correspond to the area "swept out" by the helical operator $\mathbb{S}$. Expanding, we find

$$|\mathbf{H}\times\mathbf{B}| = (m_1n_2 - m_2n_1)|\mathbf{R}_1\times\mathbf{R}_2| \qquad (1)$$

where $|\mathbf{R}_1\times\mathbf{R}_2|$ is just the area per two-carbon unit cell of the primitive graphene lattice. Thus $(m_1n_2 - m_2n_1)$ gives the number of carbon pairs required for the unit cell under helical symmetry with a helical operator generated using $\mathbf{H}$ and the conformal mapping. Given a choice for n_1 and n_2, then $(m_1n_2 - m_2n_1)$ must equal some integer value

$$(m_1n_2 - m_2n_1) = \pm N. \qquad (2)$$

Integer arithmetic then shows that the smallest magnitude nonzero value of N will be given by the greatest common divisor of n_1 and n_2. Thus, we can easily determine the helical operator $\mathbf{H}\rightarrow\mathbb{S}(h,\varphi)$ that yields

the minimum unit cell (primitive helical motif) size of $2N$ atoms, where N is the greatest common divisor of n_1 and n_2.

Next, consider the possible rotational symmetry around the helical axis. This operation is of special interest because all the rotation operations around the chain axis will commute with the helical operator $\mathcal{S}(h,\varphi)$, allowing solutions of any one-electron Hamiltonian model to be block-diagonalized into the irreducible representations of both the helical operation and the rotation operator simultaneously. We observe that the highest order rotational symmetry (and smallest possible rotation angle for such an operator) will be given by a C_N rotation operator, where N remains the greatest common divisor of n_1 and n_2[13]. This can be seen straightforwardly by considering the real lattice vector $\mathbf{B}_N$,

$$\mathbf{B}_N = (n_1/N)\mathbf{R}_1 + (n_2/N)\mathbf{R}_2. \tag{3}$$

The conformal mapping will transform this lattice operation $\mathbf{B}_N$ to a rotation of $2\pi/N$ radians around the nanotube axis, thus generating a C_N subgroup.

The rotational and helical symmetries of a nanotube defined by $\mathbf{B}$ can then be seen by using the corresponding helical and rotational symmetry operators $\mathcal{S}(h,\varphi)$ and C_N to generate the nanotube[13,14]. This is done by first introducing a cylinder of radius $|\mathbf{B}|/2\pi$. The two carbon atoms located at $d \equiv (\mathbf{R}_1 + \mathbf{R}_2)/3$ and 2d in the [0,0] unit cell of Fig. 1 are then mapped to the surface of this cylinder. The first atom is mapped to an arbitrary point on the cylinder surface, which requires that the position of the second be found by rotating this point by $2\pi(d\cdot\mathbf{B})/|\mathbf{B}|^2$ radians about the cylinder axis in conjunction with a translation $|\mathbf{d}\times\mathbf{B}|/|\mathbf{B}|$ units along this axis. The positions of these first two atoms can then be used to generate $2(N-1)$ additional atoms on the cylinder surface by $(N-1)$ successive $2\pi/N$ rotations about the cylinder axis. Altogether, these $2N$ atoms complete the specification of the helical motif which corresponds to an area on the cylinder surface given by $N|\mathbf{R}_1\times\mathbf{R}_2|$. This helical motif can then be used to tile the remainder of the nanotube by repeated operation of the helical operation defined by $\mathcal{S}(h,\varphi)$ generated by the $\mathbf{H}$ defined using eqn (2).

3. ELECTRONIC STRUCTURE OF CARBON NANOTUBES

We will now discuss the electronic structure of single-shell carbon nanotubes in a progression of more sophisticated models. We shall begin with perhaps the simplest model for the electronic structure of the nanotubes: a Hückel model for a single graphite sheet with periodic boundary conditions analogous to those imposed by the rolling up of the nanotube. We then continue by analyzing a structurally correct nanotube within a Slater-Koster sp^3 tight-binding model using the helical symmetry of the nanotube. We then finish by discussing results for both geometry optimization and band structure using first-principles local-density functional methods.

3.1 *Graphene model*

One of the simplest models for the electronic structure of the states near the Fermi level in the nanotubes is that of a single sheet of graphite (graphene) with periodic boundary conditions[10–16]. Let us consider a Slater-Koster tight-binding model[31] and assume that the nearest-neighbor matrix elements are the same as those in the planar graphene (i.e., we neglect curvature effects). The electronic structure of the nanotube will then be basically that of graphene, with the additional imposition of Born-von Karman boundary conditions on the electronic states, so that they are periodic under translations of the circumference vector $\mathbf{B}$. The electronic structure of the π-bands near the Fermi level then reduces to a Hückel model with one parameter, the $V_{pp\pi}$ hopping matrix element. This model can be easily solved, and the one-electron eigenvalues can be given as a function of the two-dimensional wavevector $\mathbf{k}$ in the standard hexagonal Brillouin zone of graphene in terms of the primitive lattice vectors $\mathbf{R}_1$ and $\mathbf{R}_2$:

$$\varepsilon(\mathbf{k}) = V_{pp\pi}\sqrt{3 + 2\cos\mathbf{k}\cdot\mathbf{R}_1 + 2\cos\mathbf{k}\cdot\mathbf{R}_2 + 2\cos\mathbf{k}\cdot(\mathbf{R}_1 - \mathbf{R}_2)} \tag{4}$$

The Born-von Karman boundary conditions then restrict the allowed electronic states to those in the graphene Brillouin zone that satisfy

$$\mathbf{k}\cdot\mathbf{B} = 2\pi m, \tag{5}$$

that m an integer[10,14,15]. In terms of the two-dimensional Brillouin zone of graphene, the allowed states will lie along parallel lines separated by a spacing of $2\pi/|\mathbf{B}|$. Fig. 3a depicts a set of these lines for the [4,3] nanotube. The reduced dimensionality of these one-electron states is analogous to those found in quantum confinement systems; we might expect that the multiple crossings of the Brillouin zone edge would lead to the creation of multiple gaps in the electronic density-of-states (DOS) as we conceptually transform graphene into a nanotube. However, as depicted in Fig. 3b, these one-electron states are actually continuous in an extended Brillouin zone picture. A direct consequence of our conclusion in the previous section—that the helical unit cell for the [4,3] nanotube would have only two carbons, the same as in graphene itself—is that the π-band in graphene will transform into a single band, rather than several.

Initially, we showed that the set of serpentine nanotubes [n,n] are metallic. Soon thereafter, Hamada *et al.*[15] and Saito *et al.*[16,17] pointed out that the periodicity condition in eqn (5) further groups the remaining nanotubes (those that cannot be constructed

from the condition $n_1 = n_2$) into one set that has moderate band gaps and a second set with small band gaps. The graphene model predicts that the second set of nanotubes would have zero band gaps, but the symmetry breaking introduced by curvature effects results in small, but nonzero, band gaps. To demonstrate this point, consider the standard reciprocal lattice vectors $\mathbf{K}_1$ and $\mathbf{K}_2$ for the graphene lattice given by $\mathbf{K}_i \cdot \mathbf{R}_j = 2\pi\delta_{ij}$. The band structure given by eqn (4) will have a band crossing (i.e., the occupied band and the unoccupied band will touch at zero energy) at the corners $\bar{K}$ of the hexagonal Brillouin zone, as depicted in Fig. 3. These six corners $\bar{K}$ of the central Brillouin zone are given by the vectors $\mathbf{k}_{\bar{K}} \equiv \pm(\mathbf{K}_1 - \mathbf{K}_2)/3$, $\pm(2\mathbf{K}_1 + \mathbf{K}_2)/3$, and $\pm(\mathbf{K}_1 + 2\mathbf{K}_2)/3$. Given our earlier definition of $\mathbf{B}$, $\mathbf{B} = n_1\mathbf{R}_1 + n_2\mathbf{R}_2$, a nanotube will have zero band gap (within the graphene model) if and only if $\mathbf{k}_{\bar{K}}$ satisfies eqn (5), leading to the condition $n_1 - n_2 = 3m$, where m is an integer. As we shall see later, when we include curvature effects in the electronic Hamiltonian, these "*metallic*" nanotubes will actually fall into two categories: the serpentine nanotubes that are truly metallic by symmetry[10,14], and quasimetallic with small band gaps[15–18].

In addition to the zero band gap condition, we have examined the behavior of the electron states in the vicinity of the gap to estimate the band gap for the moderate band gap nanotubes[13,14]. Consider a wave vector $\mathbf{k}$ in the vicinity of the band crossing point $\bar{K}$ and define $\Delta\mathbf{k} = \mathbf{k} - \mathbf{k}_{\bar{K}}$, with $\Delta k \equiv |\Delta\mathbf{k}|$. The function $\varepsilon(\mathbf{k})$ defined in eqn (4) has a cusp in the vicinity of $\bar{K}$, but $\varepsilon^2(\mathbf{k})$ is well-behaved and can be expanded in a Taylor expansion in Δk. Expanding $\varepsilon^2(\mathbf{k})$, we find

$$\varepsilon^2(\Delta k) = \tfrac{3}{4} V_{pp\pi}^2 a^2 \Delta k^2, \tag{6}$$

where $a = |\mathbf{R}_1| = |\mathbf{R}_2|$ is the lattice spacing of the honeycomb lattice. The allowed nanotube states satisfying eqn (5) lie along parallel lines as depicted in Fig. 2 with a spacing of $2\pi/B$, where $B \equiv |\mathbf{B}|$. For the nonmetallic case, the smallest band gap for the nanotube will occur at the nearest allowed point to $\bar{K}$, which will lie one third of the line spacing from $\bar{K}$. Thus, using $\Delta k = 2\pi/3B$, we find that the band gap equals[13,14]

$$E_g = 2\varepsilon(\Delta k) = \frac{2\pi}{\sqrt{3}} \frac{V_{pp\pi} a}{B} = \frac{V_{pp\pi} r_{CC}}{R_T}, \tag{7}$$

where r_{CC} is the carbon-carbon bond distance ($r_{CC} = a/\sqrt{3} \sim 1.4$ Å) and R_T is the nanotube radius ($R_T = B/2\pi$). Similar results were also obtained by Ajiki and Ando[18].

3.2 *Using helical symmetry*

The previous analysis of the electronic structure of the carbon nanotubes assumed that we could neglect curvature effects, treating the nanotube as a single graphite sheet with periodic boundary conditions imposed analogous to those in a quantum confinement problem. This level approximation allowed us to analyze the electronic structure in terms of the two-dimensional band structure of graphene. Going beyond this level of approximation will require explicit treatment of the helical symmetry of the nanotube for practical computational treatment of the electronic structure problem. We have already discussed the ability to determine the optimum choice of helical operator $\mathbb{S}$ in terms of a graphene lattice translation $\mathbf{H}$. We now examine some of the consequences of using helical symmetry and its parallels with standard band structure theory. Because the symmetry group generated by the screw operation $\mathbb{S}$ is isomorphic with the one-dimensional translation group, Bloch's theorem can be generalized so that the one-electron wavefunctions will transform under $\mathbb{S}$ according to

$$\mathbb{S}^m \psi_i(\mathbf{r};\kappa) = e^{i\kappa m} \psi_i(\mathbf{r};\kappa). \tag{8}$$

The quantity κ is a dimensionless quantity which is conventionally restricted to a range of $-\pi < \kappa \leq \pi$, a central Brillouin zone. For the case $\varphi = 0$ (i.e., $\mathbb{S}$ a pure translation), κ corresponds to a normalized quasimomentum for a system with one-dimensional translational periodicity (i.e., $\kappa \equiv kh$, where k is the traditional wavevector from Bloch's theorem in solid-state band-structure theory). In the previous analysis of helical symmetry, with $\mathbf{H}$ the lattice vector in the graphene sheet defining the helical symmetry generator, κ in the graphene model corresponds similarly to the product $\kappa = \mathbf{k} \cdot \mathbf{H}$ where $\mathbf{k}$ is the two-dimensional quasimomentum vector of graphene.

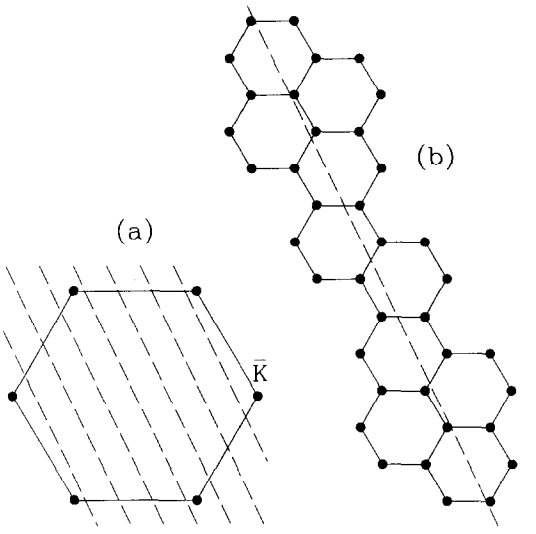

Fig. 3. (a) Depiction of central Brillouin zone and allowed graphene sheet states for a [4,3] nanotube conformation. Note Fermi level for graphene occurs at $\bar{K}$ points at vertices of hexagonal Brillouin zone. (b) Extended Brillouin zone picture of [4,3] nanotube. Note that top left hexagon is equivalent to bottom right hexagon.

Before we continue our description of electronic structure methods for the carbon nanotubes using helical symmetry, let us reconsider the metallic and quasimetallic cases discussed in the previous section in more detail. The graphene model suggests that a metallic state will occur where two bands cross, and that the Fermi level will be pinned to the band crossing. In terms of band structure theory however, if these two bands belong to the same irreducible representation of a point group of the nuclear lattice that also leaves the point in the Brillouin zone invariant, then rather than touching (and being degenerate in energy) these one-electron eigenfunctions will mix and lead to an avoided crossing. Only if the two eigenfunctions belong to different irreducible representations of the point group can they be degenerate. For graphene, the high symmetry of the honeycomb lattice allows the degeneracy of the highest-occupied and lowest-unoccupied states at the corners $\bar{K}$ of the hexagonal Brillouin zone in graphene. Rolling up graphene into a nanotube breaks this symmetry, and we must ask what point group symmetries are left that can allow a degeneracy at the band crossing rather than an avoided crossing. For the nanotubes, the appropriate symmetry operations that leave an entire band in the Brillouin zone invariant are the C_n rotation operations around the helical axis and reflection planes that contain the helical axis. We see from the graphene model that a reflection plane will generally be necessary to allow a degeneracy at the Fermi level, because the highest-occupied and lowest-unoccupied states will share the same irreducible representation of the rotation group. To demonstrate this, consider the irreducible representations of the rotation group. The different irreducible representations transform under the generating rotation (of $2\pi/N$ radians) with a phase factor an integer multiple $2\pi m/N$, where $m = 0, \ldots, N-1$. Within the graphene model, each allowed state at quasimomentum $\mathbf{k}$ will transform under the rotation by the phase factor given by $\mathbf{k}\cdot\mathbf{B}/N$, and by eqn (5) we see that the phase factor at $\bar{K}$ is just $2\pi m/N$. The eigenfunctions predicted using the graphene model are therefore already members of the irreducible representations of the rotation point group. Furthermore, the eigenfunctions at a given Brillouin zone point $\mathbf{k}$ in the graphene model must be members of the same irreducible representation of the rotation point group.

For the nanotubes, then, the appropriate symmetries for an allowed band crossing are only present for the serpentine ($[n,n]$) and the sawtooth ($[n,0]$) conformations, which will both have C_{nv} point group symmetries that will allow band crossings, and with rotation groups generated by the operations equivalent by conformal mapping to the lattice translations $\mathbf{R}_1 + \mathbf{R}_2$ and $\mathbf{R}_1$, respectively. However, examination of the graphene model shows that only the serpentine nanotubes will have states of the correct symmetry (i.e., different parities under the reflection operation) at the $\bar{K}$ point where the bands can cross. Consider the $\bar{K}$ point at $(\mathbf{K}_1 - \mathbf{K}_2)/3$. The serpentine case always satisfies eqn (5), and at the $\bar{K}$ points the one-electron wave functions transform under the generator of the rotation group C_n with a phase factor given by $\mathbf{k}_{\bar{K}}\cdot(\mathbf{R}_1 + \mathbf{R}_2) = 0$. This irreducible representation of the C_n group is split under reflection into the two irreducible representations a_1 and a_2 of the C_{nv} group that are symmetric and antisymmetric, respectively, under the reflection plane; the states at $\bar{K}$ will belong to these two separate irreducible representations. Thus, the serpentine nanotubes are always metallic because of symmetry if the Hamiltonian allows sufficient bandwidth for a crossing, as is normally the case[10]. The sawtooth nanotubes, however, present a different picture. The one-electron wave functions at $\bar{K}$ transform under the generator of the rotation group for this nanotube with a phase factor given by $\mathbf{k}_{\bar{K}}\cdot\mathbf{R}_1 = 2\pi/3$. This phase factor will belong to one of the e representations of the C_{nv} group, and the states at $\bar{K}$ in the graphene Brillouin zone will therefore belong to the same symmetry group. This will lead to an avoided crossing. Therefore, the band gaps of the nonserpentine nanotubes that satisfy eqn (5) are not truly metallic but only small band gap systems, with band gaps we estimate from empirical and first-principles calculation to be of the order of 0.1 eV or less.

Now, let us return to our discussion of carrying out an electronic structure calculation for a nanotube using helical symmetry. The one-electron wavefunctions ψ_i can be constructed from a linear combination of Bloch functions φ_j, which are in turn constructed from a linear combination of nuclear-centered functions $\chi_j(\mathbf{r})$,

$$\psi_i(\mathbf{r};\kappa) = \sum_j c_{ji}(\kappa)\varphi_j(\mathbf{r};\kappa) \tag{9}$$

$$\varphi_j(\mathbf{r};\kappa) = \sum_m e^{-i\kappa m}\mathbb{S}^m\chi_j(\mathbf{r}). \tag{10}$$

As the next step in including curvature effects beyond the graphene model, we have used a Slater-Koster parameterization[31] of the carbon valence states—which we have parameterized[32,33] to earlier LDF band structure calculations[34] on polyacetylene—in the empirical tight-binding calculations. Within the notation in ref. [31] our tight-binding parameters are given by $V_{ss\sigma} = -4.76$ eV, $V_{sp\sigma} = 4.33$ eV, $V_{pp\sigma} = 4.37$ eV, and $V_{pp\pi} = -2.77$ eV.[33] We choose the diagonal term for the carbon p orbital, $\varepsilon_p = 0$ which results in the s diagonal term of $\varepsilon_s = -6.0$ eV. This tight-binding model reproduces first-principles band structures qualitatively quite well. As an example, Fig. 4 depicts both Slater-Koster tight-binding results and first-principles LDF results[10,12] for the band structure of the [5,5] serpentine nanotube within helical symmetry. All bands have been labeled for the LDF results according to the four irreducible representations of the C_{5v} point group: the rotationally invariant a_1 and a_2 representations, and the doubly-degenerate e_1 and e_2 representation. As noted in our discussion for the ser-

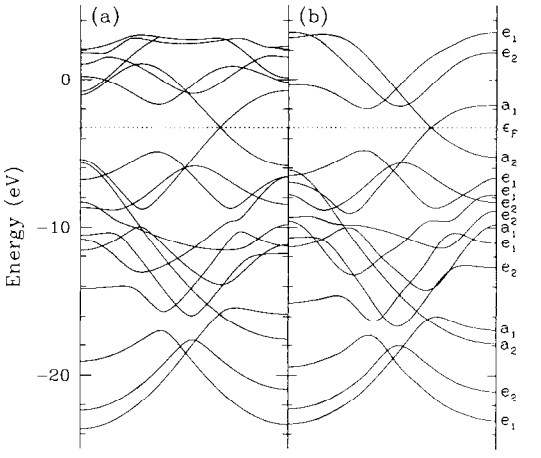

Fig. 4. (a) Slater-Koster valence tight-binding and (b) first-principles LDF band structures for [5,5] nanotube. Band structure runs from left at helical phase factor $\kappa = 0$ to right at $\kappa = \pi$. Fermi level ε_F for Slater-Koster results has been shifted to align with LDF results.

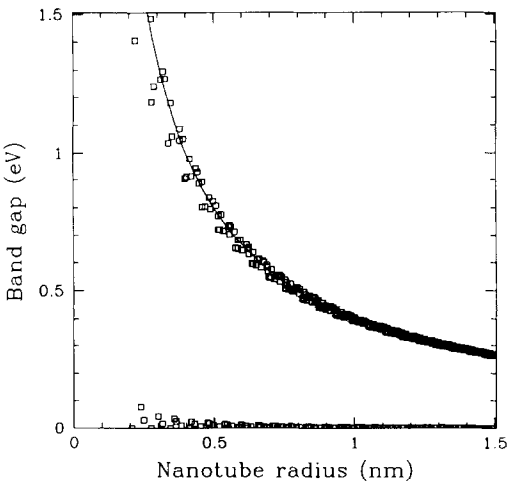

Fig. 5. Band gap as a function of nanotube radius calculated using empirical tight-binding Hamiltonian. Solid line gives estimate using Taylor expansion of graphene sheet results in eqn. (7).

pentine nanotubes, this band structure is metallic with a band crossing of the a_1 and a_2 bands.

Within the Slater-Koster approximation, we can easily test the validity of the approximations made in eqn (7) based on the graphene model. In Fig. 5 we depict the band gaps using the empirical tight-binding method for nanotube radii less than 1.5 nm. The nonmetallic nanotubes ($n_1 - n_2 \neq 3\ m$) are shown in the upper curve where we have also depicted a solid line showing the estimated band gap for the nonmetallic nanotubes using $|V_{pp\pi}| r_{CC}/R_T$, with $V_{pp\pi}$ as given above and $r_{CC} = 1.44$ Å. We see excellent agreement between the estimate based on the graphene sheet and the exact calculations for the tight-binding model with curvature introduced, with the disagreement increasing with increasing curvature at the smaller radii.

3.3 *First-principles methods*

We have extended the linear combination of Gaussian-type orbitals local-density functional approach to calculate the total energies and electronic structures of helical chain polymers[35]. This method was originally developed for molecular systems[36–40], and extended to two-dimensionally periodic systems[41,42] and chain polymers[34]. The one-electron wavefunctions here ψ_i are constructed from a linear combination of Bloch functions φ_j, which are in turn constructed from a linear combination of nuclear-centered Gaussian-type orbitals $\chi_j(\mathbf{r})$ (in this case, products of Gaussians and the real solid spherical harmonics). The one-electron density matrix is given by

$$\rho(\mathbf{r};\mathbf{r}') = \sum_i \frac{1}{2\pi} \int_{-\pi}^{\pi} d\kappa n_i(\kappa) \psi_i^*(\mathbf{r}';\kappa) \psi_i(\mathbf{r};k)$$

$$= \sum_{jj'} \sum_m P_{j'j}^m \sum_{m'} \chi_{j'}^{m+m'}(\mathbf{r}') \chi_j^{m'}(\mathbf{r}), \qquad (11)$$

where $n_i(\kappa)$ are the occupation numbers of the one-electron states, χ_j^m denotes $\mathcal{S}^m \chi_j(\mathbf{r})$, and P_{ij}^m are the coefficients of the real lattice expansion of the density matrix given by

$$P_{j'j}^m = \sum_i \frac{1}{2\pi} \int_{-\pi}^{\pi} d\kappa n_i(\kappa) c_{j'i}^*(\kappa) c_{ji}(\kappa) e^{i\kappa m} \qquad (12)$$

The total energy for the nanotube is then given by

$$E = \sum_{ij} \sum_m P_{ij}^m \left\{ -\frac{1}{2} \left\langle \chi_i^m \middle| \nabla^2 \middle| \chi_j^0 \right\rangle + \left\langle \chi_i^m \middle| \varepsilon_{xc}[\rho(\mathbf{r})] \middle| \chi_j^0 \right\rangle \right\}$$

$$+ \frac{1}{2} \sum_{m''} \left\{ \left(\sum_n {}' \sum_{n'} \frac{Z_n Z_{n'}}{|\mathbf{R}_n^0 - \mathbf{R}_{n'}^{m''}|} \right) + \sum_{ij} \sum_m P_{ij}^m \left(\sum_{i'j'} \sum_{m'} P_{i'j'}^{m'} [\chi_i^m \chi_j^0 | \chi_{i'}^{m'+m''} \chi_{j'}^{m''}] - 2 \sum_n \left\langle \chi_i^m \middle| \frac{Z_n}{|\mathbf{r} - \mathbf{R}_n^{m''}|} \middle| \chi_j^0 \right\rangle \right) \right\} \qquad (13)$$

where Z_n and $\mathbf{R}_n$ denote the nuclear charges and coordinates within a single unit cell, $\mathbf{R}_n^m$ denotes the nuclear coordinates in unit cell m ($\mathbf{R}_n^m \equiv \mathcal{S}^m \mathbf{R}_n$), and $[\rho_1|\rho_2]$ denotes an electrostatic interaction integral,

$$[\rho_1|\rho_2] \equiv \int d^3 r_1 \int d^3 r_2 \frac{\rho_1(\mathbf{r}_1)\rho_2(\mathbf{r}_2)}{r_{12}} \qquad (14)$$

Rather than solve for the total energy directly as expressed in eqn (13), we follow the suggestion of ear-

lier workers to fit the exchange-correlation potential and the charge density (in the Coulomb potential) to a linear combination of Gaussian-type functions.

We have carried out a series of geometry optimizations on nanotubes with diameters less than 2 nm. We will present some results for a selected subset of the moderate band gap nanotubes, and then focus on results for an example chiral systems: the chiral [9,2] nanotube with a diameter of 0.8 nm. This nanotube has been chosen because its diameter corresponds to those found in relatively large amounts by Iijima[7] after the synthesis of single-walled nanotubes.

How the structural properties of the fullerene nanotubes change with conformation is one of the most important questions to be answered about these new materials. In particular, two properties are most apt for study with the LDF approach: how does the band gap change with nanotube diameter, and how does the strain energy change with nanotube diameter? We have studied these questions extensively using empirical methods[10–14,23], and are currently working on a comprehensive study of the band gaps, strain energies, and other properties using the LDF approach. We expect from eqn (7) and the previous analysis of the graphene sheet model that the moderate band gap nanotubes should have band gaps that vary roughly inversely proportional to the nanotube radius. In Fig. 6 we depict representative results for some moderate band gap nanotubes. In the figure, we see that not only do our first-principles band gaps decrease in an inverse relationship to the nanotube radius, but that the band gaps are well described with a reasonable value of $V_{pp\pi} \sim -2.5$ eV.

Second, we expect that the strain energy per carbon should increase inversely proportional to the square of the nanotube radius[23]. Based on a continuum elastic model, Tibbetts[4] derived a strain energy for a thin graphitic nanotube of the general form:

$$\sigma = \frac{\pi E L a^3}{12R} \tag{16}$$

where E is the elastic modulus, R is the radius of curvature, L is the length of the cylinder, and a is a representative thickness of the order of the graphite interplanar spacing (3.35 Å). Assuming that the total number of carbons is given by $N = 2\pi RL/\Omega$, where Ω is the area per carbon, we find that the strain energy per carbon is expected to be

$$\frac{\sigma}{N} = \frac{Ea^3}{24}\frac{\Omega}{R^2}. \tag{17}$$

In earlier work, we found this relationship was well observed, using empirical bond-order potentials for all nanotubes with radii less than 0.9 nm, and for a range of serpentine nanotubes using the LDF method. As part of our studies, we have carried out first-principles LDF calculations on a representative sample of chiral nanotubes. Iijima and Ichihashi[7] have recently reported the synthesis of single-shell fullerene nanotubes with diameters of about 1 nm, using the gas-phase product of a carbon-arc synthesis with iron vapor present. After plotting the frequency of single-shell nanotubes they observed versus nanotube diameter, they found enhanced abundances for diameters of roughly 0.8 nm and 1.1 nm. For first-principles simulations then to be useful, they should be capable of calculations for nanotubes with diameters from about 0.6–2.0 nm. In Fig. 7 we depict the calculated total energy per carbon, shifted relative to an extrapolated value for an infinite radius nanotube, for a representative sample of nanotubes over this range using the LDF approach. In this figure, the open squares denote results for unoptimized nanotubes, where the nano-

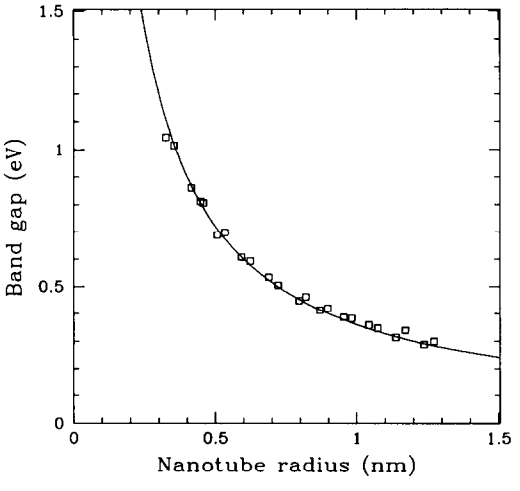

Fig. 6. Band gap as a function of nanotube radius using first-principles LDF method. Solid line shows estimates using graphene sheet model with $V_{pp\pi} = -2.5$ eV.

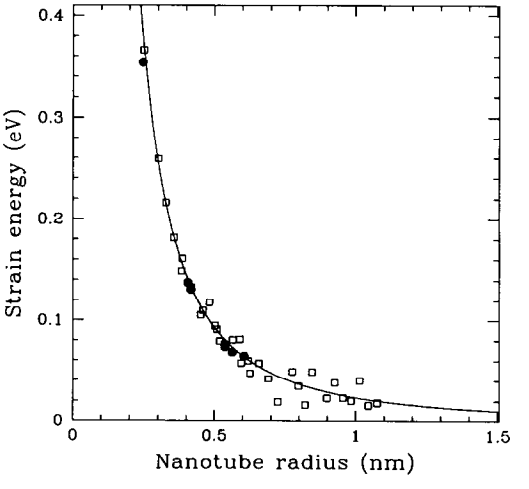

Fig. 7. Strain energy per carbon (total energy minus total energy extrapolated for the graphite sheet) as a function of nanotube radius calculated for unoptimized nanotube structures (open squares) and optimized nanotube structures (solid circles). Solid line depicts inverse square relationship drawn through point at smallest radius.

Table 1. Relaxation energy per carbon (eV) obtained by geometry optimization of nanotubes relative to extrapolated value for graphene

Nanotube	Radius (nm)	Unrelaxed energy (eV)	Relaxed energy (eV)
[12,5]	0.6050	0.067	0.064
[13,2]	0.5630	0.071	0.068
[11,4]	0.5370	0.076	0.073
[7,5]	0.4170	0.133	0.130
[9,2]	0.4060	0.140	0.137
[4,3]	0.2460	0.366	0.354

tube has been directly constructed from a conformal mapping of graphene with a carbon-carbon nearest-neighbor distance of 0.144 nm. We have carried out a limited number of complete geometry optimizations within the LDF approach. All of the nanotubes selected fall in the range of radii from 0.4–0.6 nm representative of the relatively high abundances found by Iijima and Ichihashi[7]. For the nanotubes studied, the change in energy resulting from relaxation of the lattice is minimal, as depicted by the solid circles in Fig. 7, and presented in Table 1. We see the inverse square relationship is still well observed, although at the larger nanotube radii we begin to observe some scatter in the results that arises from the numerical roundoff errors.

As an example of a nanotube representative of the diameters experimentally found in abundance, we have calculated the electronic structure of the [9,2] nanotube, which has a diameter of 0.8 nm. Figure 8 depicts the valance band structure for the [9,2] nanotube. This band structure was calculated using an unoptimized nanotube structure generated from a conformal mapping of the graphite sheet with a 0.144 nm bond distance. We used 72 evenly-spaced points in the one-dimensional Brillouin zone ($-\pi < \kappa \leq \pi$) and a carbon 7s3p Gaussian basis set. Our earlier analysis of the graphene sheet model predicts that each band of the graphene sheet transforms to a single band of the [9,2] nanotube. From our earlier work[11–14] we expect a highly oscillatory band structure (using the helical symmetry) with about 12 oscillations in each band over the Brillouin zone. In Fig. 8, we see basically six local maxima in each band in the half Brillouin zone depicted. Further, we see the band gap at about one third of the way from the left-hand side of Fig. 8. The highly oscillatory nature of the band structure in these nanotubes makes accurate measurement of the band gap difficult. In our current studies of the band gap of these materials, we typically perform the self-consistent portion of the calculations with a modest number of evenly-spaced points in the Brillouin zone (usually 72 for the entire Brillouin zone). We then perform non-self-consistent calculations of the band structure, using the charge density and exchange potential calculated, for more densely spaced points in the vicinity of the band gap. An example of this is depicted in Fig. 9, which shows the direct gap of the [9,2] nanotube in the vicinity of the band gap. We see that our predicted band gap for the [9,2] nanotube is 0.9 eV.

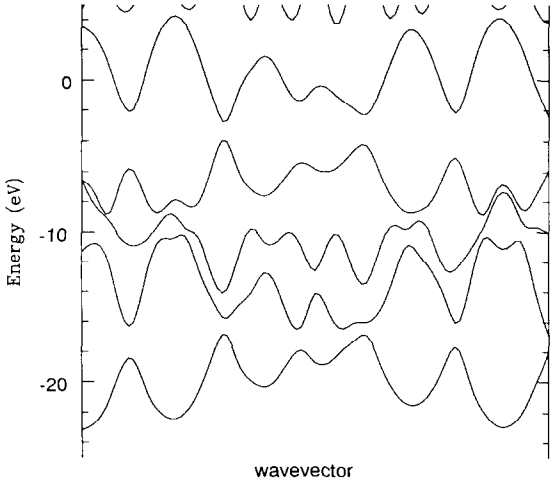

Fig. 8. LDF valence band structure of [9,2] chiral nanotube. The Fermi level lies at midgap at −3.3 eV. Dimensionless wavenumber coordinate κ ranges from 0 to π.

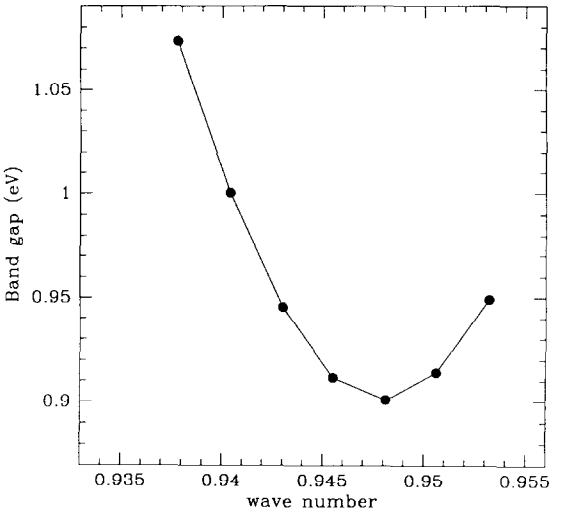

Fig. 9. Direct band gap for [9,2] nanotube in vicinity of band gap. Wave number is dimensionless coordinate κ, with one-dimensional Brillouin zone for κ defined $-\pi \leq \kappa \leq \pi$.

4. SUMMARY

Both in work reviewed herein and in theoretical research by other workers[10–30], a consensus has been reached that anomalous properties (compared to graphite and "*normal*" graphitic nanotubes) can be obtained with graphitic nanotubes with diameters of the order of a nanometer. In terms of electronic properties, the nanotubes are expected to fall into two major classes: on one hand the moderate band gap nanotubes that do not satisfy the $n_1 - n_2 = 3\,m$ condition in the

graphene sheet, and on the other hand the small band gap and truly metallic serpentine conformation nanotubes that do satisfy this condition. We have earlier demonstrated[10–12] for the serpentine nanotubes that, for diameters under a nanometer, we expect that the density of states at the Fermi level is comparable to metallic densities and that the nanotubes should not Peierls-distort at normal temperatures. Independent of helicity, we find that the larger-diameter moderate band gap members of the family of moderate band gap nanotubes ($n_1 - n_2 \neq 3\ m$) have bandgaps given approximately by $E_g = |V_{pp\pi}|(r_{CC}/R_T)$ and hence do not have bandgaps approaching k_BT at room temperature until their diameters exceed approximately about 30 nm[10].

We have also examined the energetics and elastic properties of small-diameter graphitic nanotubes using both first-principles and empirical potentials[23]. We find that the strain energy per carbon relative to an unstrained graphite sheet goes as $1/R_T^2$ (where R_T is the nanotube radius) and is insensitive to other aspects of the lattice structure, indicating that relationships derivable from continuum elastic theory persist well into the small radius limit. In general, we find that the elastic properties are those expected by directly extrapolating the behavior of larger graphitic fibers to a small cross-section.

The recent advances in synthesis of single-shell nanotubes should stimulate a wealth of new experimental and theoretical studies of these promising materials aimed at determining their structural, electronic, and mechanical properties. Many questions remain to be further investigated. How can they be terminated[29,43] and can they be connected[30]? What are their electrical properties? For those that are semiconductors, can they be successfully doped[44]? What are the mechanical properties of these nanotubes? How will they respond under compression and stress[23–28]? Do they have the high strengths and rigidity that their graphitic and tubular structure implies? How are these nanotubes formed[43,45,46]? Can techniques be devised that optimize the growth and allow the extraction of macroscopic amounts of selected nanotubes[7,8]? These questions all deserve immediate attention, and the promise of these novel all-carbon materials justify this as a major research area for the current decade.

Acknowledgements—This work was supported by the Office of Naval Research (ONR) through the Naval Research Laboratory and directly through the ONR (Chemistry-Physics and Materials Divisions. We thank D. H. Robertson, D. W. Brenner, and B. I. Dunlap for many useful discussions.

REFERENCES

1. S. Iijima, *Nature* (London) **354**, 56 (1991).
2. W. Krätschmer, L. D. Lamb, K. Fostiropoulos, and D. R. Huffman, *Chem. Phys. Lett.* **170**, 167 (1990). *Nature* **347**, 354 (1990).
3. W. E. Billups and M. A. Ciufolini, eds. *Buckminsterfullerenes*. VCH, New York (1993).
4. G. G. Tibbetts, *J. Crystal Growth* **66**, 632 (1983).
5. J. S. Speck, M. Endo, and M. S. Dresselhaus, *J. Crystal Growth* **94**, 834 (1989).
6. T. W. Ebbesen and P. M. Ajayan, *Nature* (London) **358**, 220 (1992).
7. S. Iijima and T. Ichihashi, *Nature* (London) **363**, 603 (1993).
8. D. S. Bethune, C. H. Klang, M. S. DeVries, G. Gorman, R. Savoy, J. Vazquez, and R. Beyers, *Nature* (London) **363**, 605 (1993).
9. M. Endo, K. Takeuchi, S. Igarashi, K. Kobori, M. Shiraishi, and H. W. Kroto, *J. Phys. Chem. Solids* **54**, 1841 (1993).
10. J. W. Mintmire, B. I. Dunlap, and C. T. White, *Phys. Rev. Lett.* **68**, 631 (1992).
11. C. T. White, J. W. Mintmire, R. C. Mowrey, D. W. Brenner, D. H. Robertson, J. A. Harrison, and B. I. Dunlap, In *Buckminsterfullerenes* (Edited by W. E. Billups and M. A. Ciufolini) pp. 125–184. VCH, New York, (1993).
12. J. W. Mintmire, D. H. Robertson, B. I. Dunlap, R. C. Mowrey, D. W. Brenner, and C. T. White, *Electrical, Optical, and Magnetic Properties of Organic Solid State Materials* (Edited by L. Y. Chiang, A. F. Garito, and D. J. Sandman) p. 339. MRS Symposia Proceedings No. 247. Materials Research Society, Pittsburgh (1992).
13. C. T. White, D. H. Robertson, and J. W. Mintmire, *Phys. Rev. B* **47**, 5485 (1993).
14. J. W. Mintmire, D. H. Robertson, and C. T. White, *J. Phys. Chem. Solids* **54**, 1835 (1993).
15. N. Hamada, S. Sawada, and A. Oshiyamu, *Phys. Rev. Lett.* **68**, 1579 (1992).
16. R. Saito, M. Fujita, G. Dresselhaus, M. S. Dresselhaus, *Phys. Rev. B* **46**, 1804 (1992). *Mater. Res. Soc. Sym. Proc.* **247**, 333 (1992); *Appl. Phys. Lett.* **60**, 2204 (1992).
17. R. Saito, G. Dresselhaus, and M. S. Dresselhaus, *J. Appl. Phys.* **73**, 494 (1993).
18. H. Ajiki and T. Ando, *J. Phys. Soc. Japan* **62**, 1255 (1993). *J. Phys. Soc. Japan* **62**, 2470 (1993).
19. P.-J. Lin-Chung and A. K. Rajagopal, *J. Phys. C* **6**, 3697 (1994). *Phys. Rev. B* **49**, 8454 (1994).
20. X. Blase, L. X. Benedict, E. L. Shirley, and S. G. Louie, *Phys. Rev. Lett.* **72**, 1878 (1994).
21. D. J. Klein, W. A. Seitz, and T. G. Schmalz, *J. Phys. Chem.* **97**, 1231 (1993).
22. K. Harigaya, *Phys. Rev. B* **45**, 12071 (1992).
23. D. H. Robertson, D. W. Brenner, and J. W. Mintmire, *Phys. Rev. B* **45**, 12592 (1992).
24. A. A. Lucas, P. H. Lambin, and R. E. Smalley, *J. Phys. Chem. Solids* **54**, 587 (1993).
25. J.-C. Charlier and J.-P. Michenaud, *Phys. Rev. Lett.* **70**, 1858 (1993).
26. G. Overney, W. Zhong, and D. Tománek, *Z. Phys. D* **27**, 93 (1993).
27. R. S. Ruoff, J. Tersoff, D. C. Lorents, S. Subramoney, and B. Chan, *Nature* **364**, 514 (1993).
28. J. Tersoff and R. S. Ruoff, *Phys. Rev. Lett.* **73**, 676 (1994).
29. M. Fujita, R. Saito, G. Dresselhaus, M. S. Dresselhaus, *Phys. Rev. B* **45**, 13834 (1992).
30. B. I. Dunlap, *Phys. Rev. B* **46**, 1933 (1992).
31. J. C. Slater and G. F. Koster, *Phys. Rev.* **94**, 1498 (1954).
32. M. L. Elert, J. W. Mintmire, and C. T. White, *J. Phys. (Paris), Colloq.* **44**, C3-451 (1983).
33. M. L. Elert, C. T. White, and J. W. Mintmire, *Mol. Cryst. Liq. Cryst.* **125**, 329 (1985). C. T. White, D. H. Robertson, and J. W. Mintmire, unpublished.
34. J. W. Mintmire and C. T. White, *Phys. Rev. Lett.* **50**, 101 (1983). *Phys. Rev. B* **28**, 3283 (1983).
35. J. W. Mintmire, In *Density Functional Methods in Chemistry* (Edited by J. Labanowski and J. Andzelm) p. 125. Springer-Verlag, New York (1991).
36. B. I. Dunlap, J. W. D. Connolly, and J. R. Sabin, *J.*

Chem. Phys. **71**, 3396 (1979). *J. Chem. Phys.* **71**, 4993 (1979).
37. J. W. Mintmire, *Int. J. Quantum Chem. Symp.* **13**, 163 (1979).
38. J. W. Mintmire and J. R. Sabin, *Chem. Phys.* **50**, 91 (1980).
39. J. W. Mintmire and B. I. Dunlap, *Phys. Rev. A* **25**, 88 (1982).
40. J. W. Mintmire, *Int. J. Quantum Chem. Symp.* **24**, 851 (1990).
41. J. W. Mintmire and J. R. Sabin, *Int. J. Quantum Chem. Symp.* **14**, 707 (1980).
42. J. W. Mintmire, J. R. Sabin, and S. B. Trickey, *Phys. Rev. B* **26**, 1743 (1982).
43. S. Iijima, *Mater. Sci. Eng.* **B19**, 172 (1993).
44. J.-Y. Yi and J. Bernholc, *Phys. Rev. B* **47**, 1703 (1993).
45. M. Endo and H. W. Kroto, *J. Phys. Chem.* **96**, 6941 (1992).
46. S. Iijima, P. M. Ajayan, and T. Ichihashi, *Phys. Rev. Lett.* **69**, 3100 (1992).